

# Supporting Information for

## Structural and Optical Properties of Discrete Dendritic Pt Nanoparticles on Colloidal Au Nanoprisms

*Rowan K. Leary,<sup>1</sup> Anjali Kumar,<sup>2</sup> Patrick J. Straney,<sup>3</sup> Sean M. Collins,<sup>1</sup> Sadegh Yazdi,<sup>5</sup> Rafal E. Dunin-Borkowski,<sup>4</sup> Paul A. Midgley,<sup>1</sup> Jill E. Millstone,<sup>3</sup> Emilie Ringe<sup>2,5</sup>*

1. Department of Materials Science and Metallurgy, University of Cambridge, 27 Charles Babbage Road, Cambridge CB3 0FS, UK

2. Department of Chemistry, Rice University, 6100 Main St., Houston TX 77005, USA

3. Department of Chemistry, University of Pittsburg, 219 Parkman Avenue, Pittsburg PA 15260, USA

4. Ernst Ruska-Centre for Microscopy and Spectroscopy with Electrons (ER-C) and Peter Grünberg Institut 5 (PGI-5), Forschungszentrum Jülich GmbH, D-52425 Jülich, Germany

5. Department of Materials Science and NanoEngineering, Rice University, 6100 Main St., Houston TX 77005, USA

## S1. Additional Images and EDS Elemental Maps

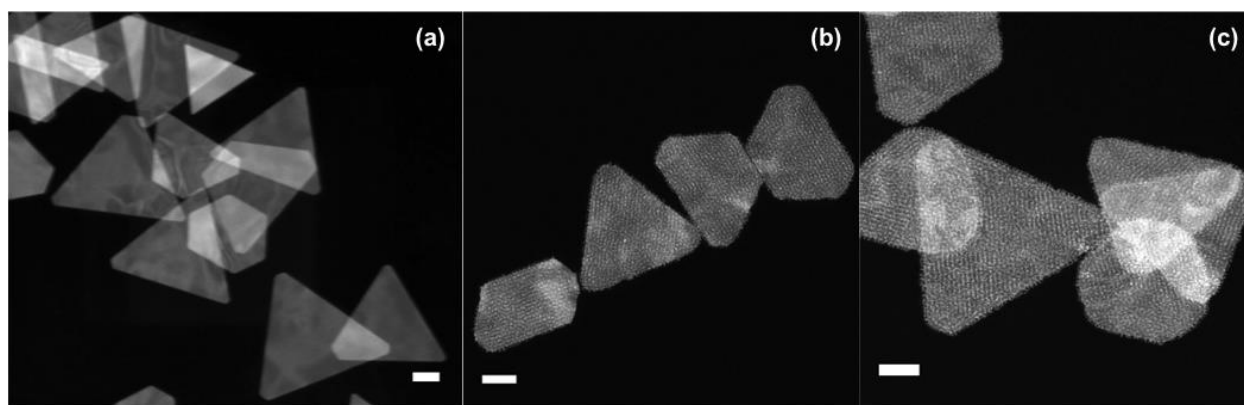


**Figure S1.** Additional HAADF-STEM images of nanoprisms (a) before and (b, c) after deposition of Pt NPs. Scale bars, 50 nm.

The Energy dispersive X-ray spectroscopy (EDS) maps presented in Figure 1 of the manuscript were obtained by summing the  $L_{\alpha}$  and  $L_{\beta 1}$  intensities for Pt and Au. X-ray emission occurs at 9.44, 11.07, 9.71, and 11.44 keV for Pt  $L_{\alpha}$ , Pt  $L_{\beta 1}$ , Au  $L_{\alpha}$ , and Au  $L_{\beta 1}$ , respectively. The M lines were not used because of the significant energy overlap of Au and Pt lines. Figure S2 shows the individual, background subtracted line maps, as well as the difference of the total ( $L_{\alpha} + L_{\beta 1}$ ) signal of Pt and Au. The latter confirms the presence of solely Pt at the edges of the particle, i.e., where the Pt nanoparticles (NPs) extend beyond the Au support.

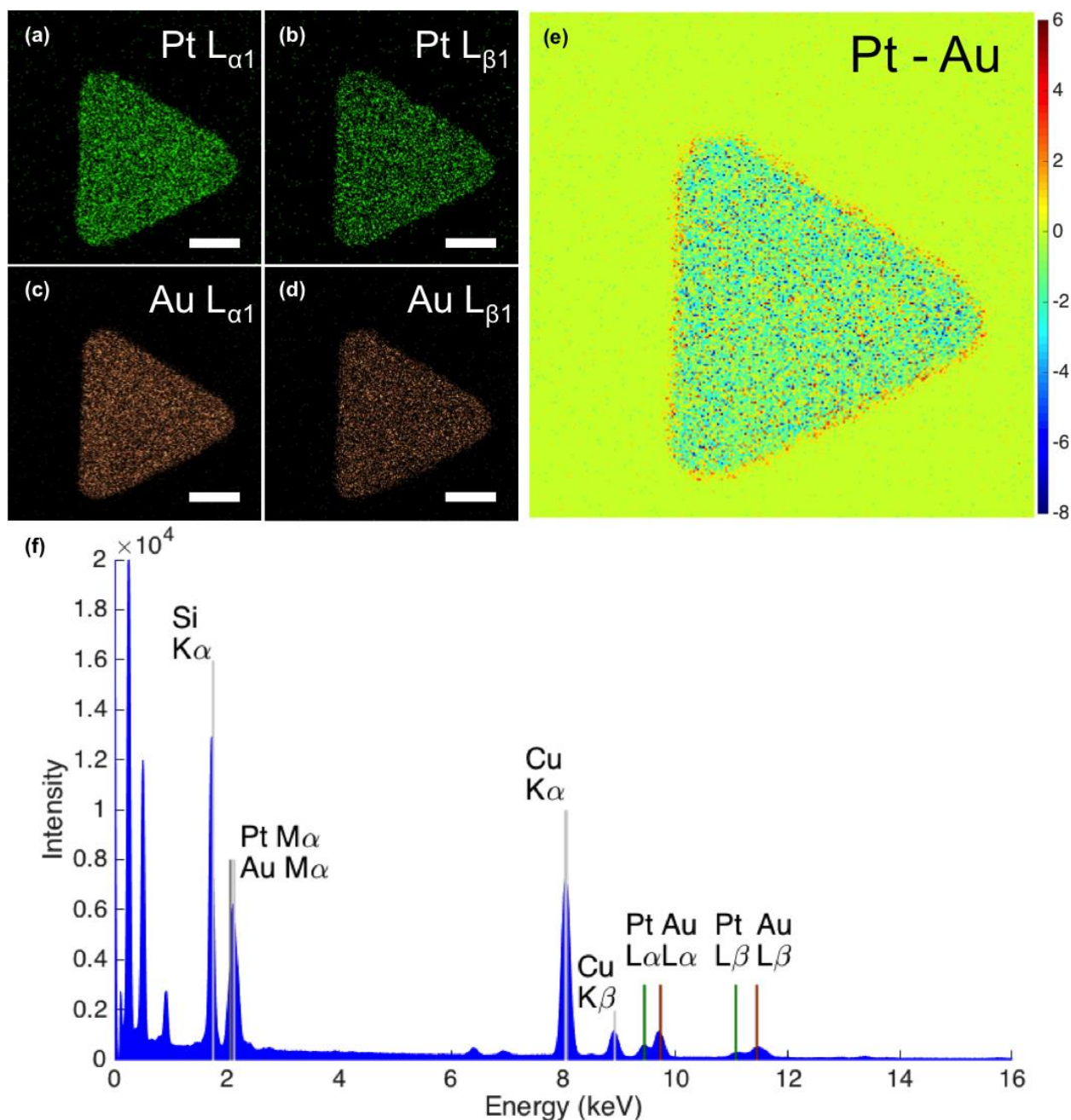


**Figure S2.** Additional EDS data for the Pt-decorated Au nanoprism shown in Figure 1. (a-d) STEM-EDS maps of the Au and Pt  $L_{\alpha}$  and  $L_{\beta 1}$  lines. For clarity the contrast was enhanced by saturating 0.3% of the pixels (no contrast enhancement in the manuscript). (e) Difference between Au and Pt intensity. The lime green background indicates a value of zero, in this case because there is no signal for either Au or Pt. The red/orange outline shows significantly more Pt signal than Au. (f) Spectrum, summed over the spatial axes of the full EDS spectrum image. Scale bars, 50 nm.

## S2. Additional Electron Tomography Visualization and Interpretation

As noted in the manuscript it is widely accepted<sup>1</sup> that HAADF-STEM imaging provides, to a generally sufficient approximation, a “projection” amenable to tomographic reconstruction. Nevertheless, some violation of the monotonically varying projection intensity and a number of other matters that influence the tomographic reconstruction process should be considered when rigorously interpreting the reconstructions. Although providing many valuable insights into the 3D morphology of the Au-Pt nanoprisms, as described in the manuscript, it should be borne in mind that the tomograms do not correspond to perfect 3D reconstructions. For the benefit of the reader less acquainted with electron tomography, and because many of the matters are not readily quantified or singly attributable, further discussion of the fidelity of the tomographic reconstructions is provided here, including most probable contributing factors.

Although HAADF-STEM imaging can provide atomic number contrast (approaching a  $Z^2$  relationship), this would be expected to be minimal in the reconstructions here, given the very close atomic numbers of Au and Pt (79 and 78 respectively). Further, if both the Au nanoprism and Pt NPs were of constant density, the reconstructions would again be expected to show a single intensity in the orthoslices. Contrary to these expectations, it is apparent that in many regions, the reconstructions show inhomogeneous intensity across the Au nanoprism. Also, many of the Pt NPs are considerably brighter than the Au nanoprism. However, rather than the observed variations in intensity reflecting significant density differences, we attribute them as dominantly due to non-linearity in the projection images and imperfections in the tomographic reconstruction process, described below.

Viewing the aligned tilt series (Movies 1-4), considerable local diffraction contrast occurs at certain tilt angles, which corrupts the monotonic mass-thickness dependence of the HAADF signal. This will in turn have an impact on the tomographically reconstructed intensity and morphology. It is also apparent that the nanoprisms sometimes “wobble” (unwanted tilting different to the applied tilt), that there is warping of some of the images (most likely due to charging effects) and there are tearing artefacts in some images (due to charging and beam scanning imperfections). These factors also corrupt the reconstructions directly, and further so by prohibiting perfect alignment of the tilt series images. The finite number of projections means that these artefacts still manifest in the reconstructions; i.e. they are not negated by an effective averaging when many projections contribute to a tomographic reconstruction.

It should also be noted that the boundaries of the Au nanoprism and Pt NPs are not pristinely defined. This is due partially to the limited tilt range, which leads to a false elongation in the beam direction;<sup>1</sup> although this well-known artifact has been markedly reduced in the reconstructions here through the use of compressed sensing based reconstruction employing total variation minimization (thorough description of total variation minimization and its implementation in electron tomographic reconstruction can be found elsewhere<sup>2-5</sup>). The artifacts of the previous paragraph also contribute to reduced definition of the Au nanoprism and Pt NPs, especially the strong diffraction contrast and wobbling of the nanoprism, which we interpret as leading to some considerable, though generally distinguishable, false intensity above and below the true nanoprism surface. We also suggest that these lead to some apparent non-flatness of the nanoprism surface.

Viewing the tilt series and other HAADF images it is visible that the Pt NPs appear very bright when NPs on either side of the Au nanoprism overlap, as would be expected for a

thickness-dependent signal. We suggest that the effects described previously reduce the reconstructed intensity of the Au nanoprism, while the Pt NPs remain bright, especially due to their strong brightness in many of the images.

A further probable artifact is the presence of striations in the Au nanoprisms (see central orthoslices), which probably result from the bright Pt NP effect in most cases, though some striations and inhomogeneous intensity in the Au nanoprism may result from other sources such as the tearing artifacts and local diffraction contrast discussed above.

The alignment challenges in particular will distort the Pt NP morphologies to some degree, but in the majority of cases not sufficiently so to prevent analysis of their general form, such as “stump”, “uncapped trunk” or “mushroom-like”, nor of their spatial distribution.

Despite the considerable challenges outlined, it is clear from the reconstructions that many valuable and genuine features of the Au nanoprisms and decorating Pt NPs are revealed. The visualizations provided in the manuscript have been carefully chosen to best represent features and morphology judged to be genuine, though should always be viewed with the points outlined here in mind.

Further visualization of the electron tomography reconstructions is provided in Figures S3-6 and Movies 1-12.

Movies 1-4: Tilt series images for the Pt-decorated Au nanoprism tomography reconstructions shown in Figures 2(a-d) and S3-6. (AVI files: jp6b02103\_si\_002, jp6b02103\_si\_003, jp6b02103\_si\_004, jp6b02103\_si\_005).

Movies 5-8: Sequential orthoslices in the x-y plane of the Pt-decorated Au nanoprism tomography reconstructions shown in Figures 2(a-d) and S3-6. (AVI files: jp6b02103\_si\_006, jp6b02103\_si\_007, jp6b02103\_si\_008, jp6b02103\_si\_009).

Movies 9-12: Rotating volume rendering visualizations of the Pt-decorated Au nanoprism tomography reconstructions shown in Figures 2(a-d) and S3-6. (AVI files: jp6b02103\_si\_010, jp6b02103\_si\_011, jp6b02103\_si\_012, jp6b02103\_si\_013).

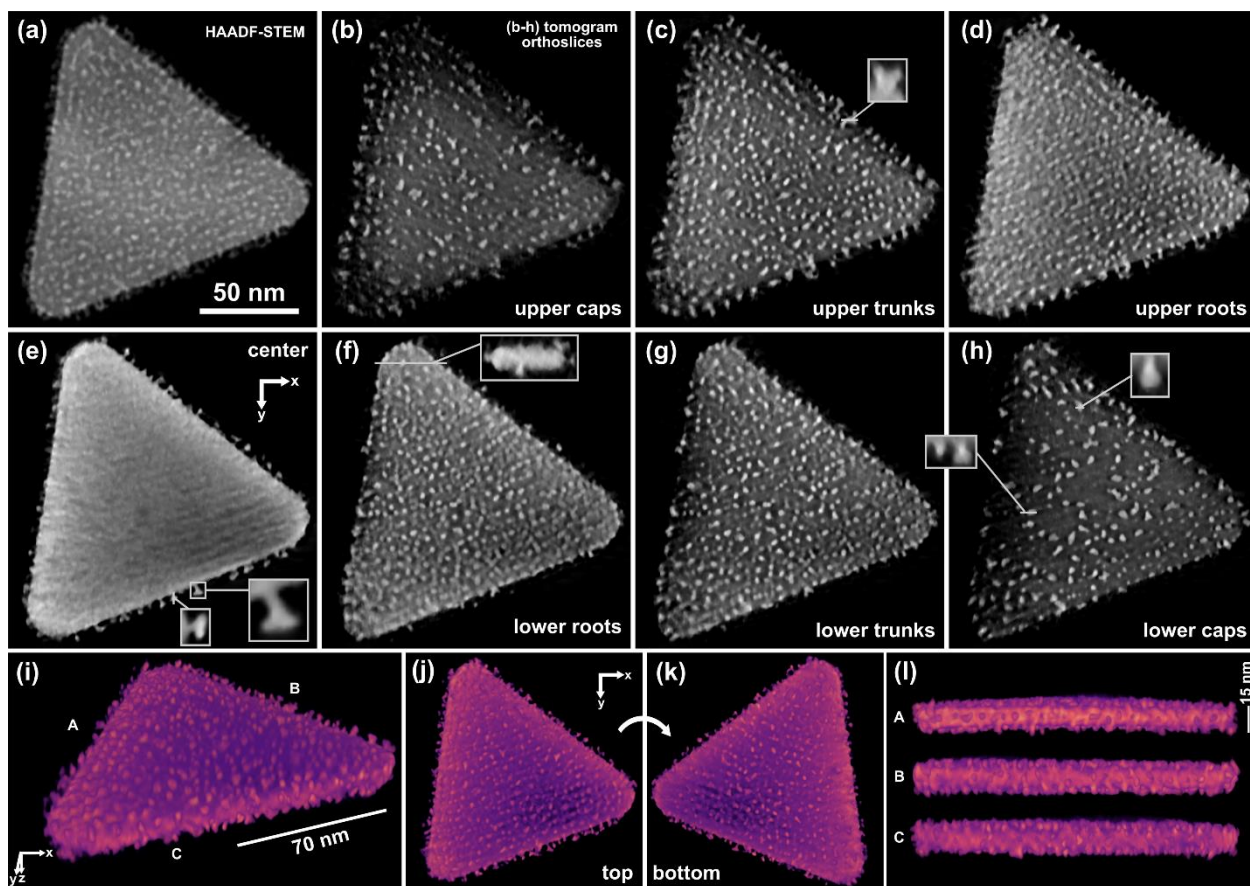


**Figure S3.** Corresponding HAADF-STEM image (a), along with additional orthoslices (b-h) and volume rendering visualizations (i-l) of the Pt-decorated Au nanoprism tomographic reconstruction shown in Figure 2(a) of the manuscript.

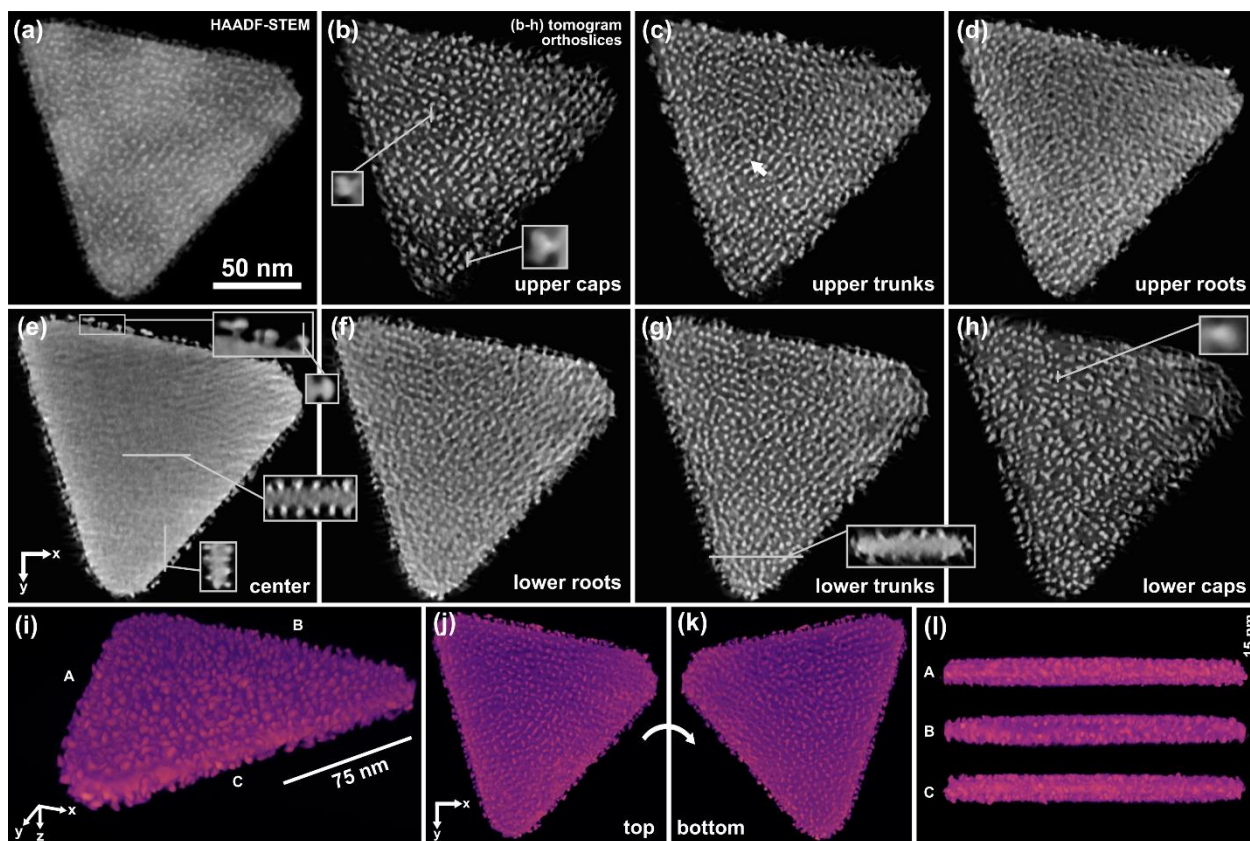


**Figure S4.** Corresponding HAADF-STEM image (a), along with additional orthoslices (b-h) and volume rendering visualizations (i-l) of the Pt-decorated Au nanoprism tomographic reconstruction shown in Figure 2(b) of the manuscript. The arrow in (c) indicates an example of circular arrangement of the Pt NPs.

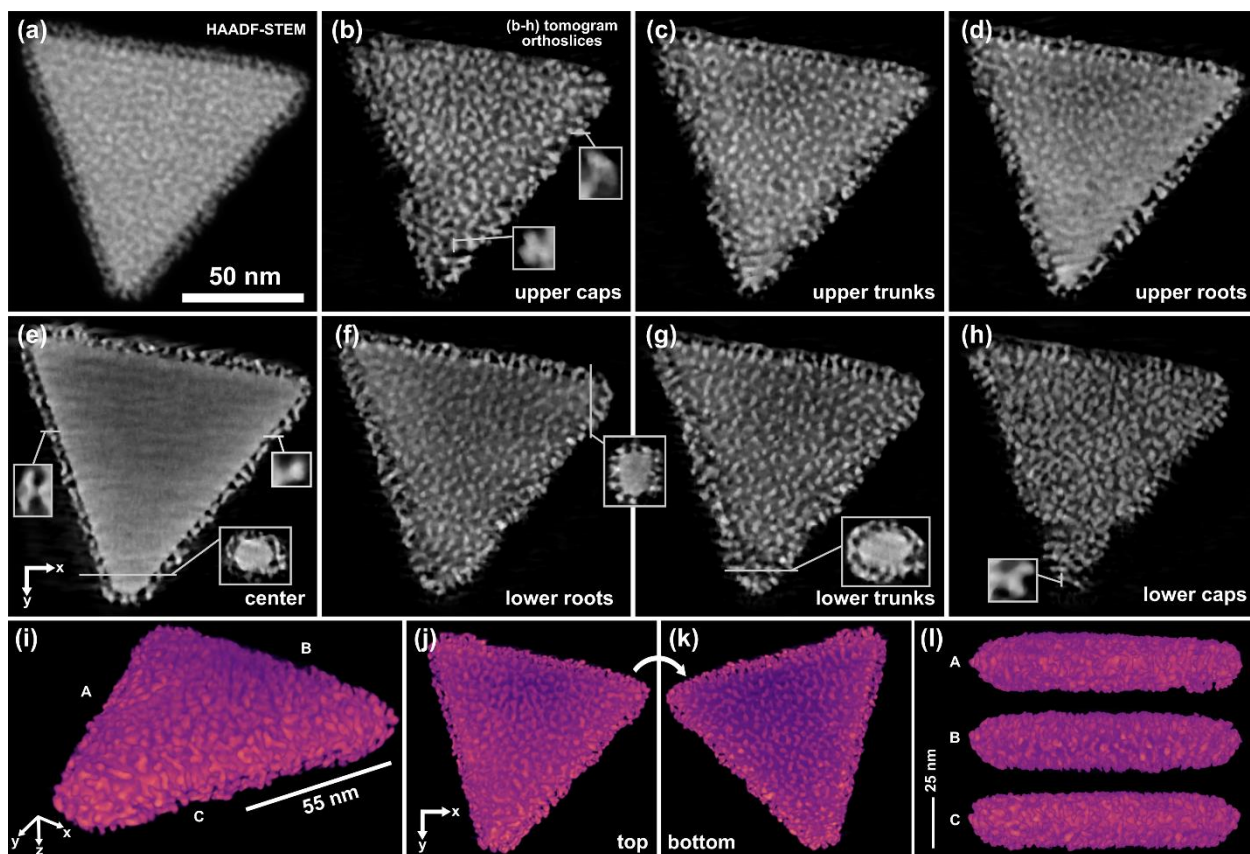


**Figure S5.** Corresponding HAADF-STEM image (a), along with additional orthoslices (b-h) and volume rendering visualizations (i-l) of the Pt-decorated Au nanoprism tomographic reconstruction shown in Figure 2(c) of the manuscript.

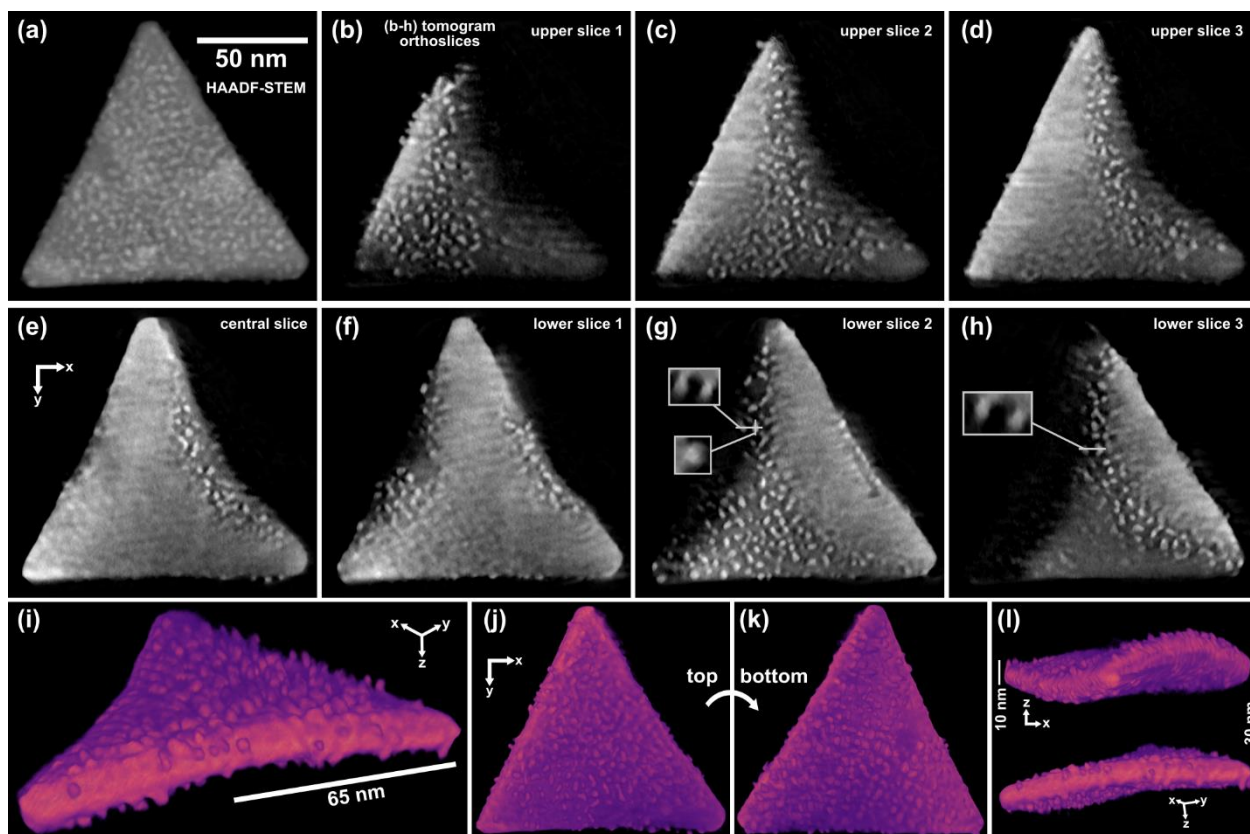


**Figure S6.** Corresponding HAADF-STEM image (a), along with additional orthoslices (b-h) and volume rendering visualizations (i-l) of the Pt-decorated Au nanoprism tomographic reconstruction shown in Figure 2(d) of the manuscript.

### S3. UV-Vis-NIR Spectroscopy

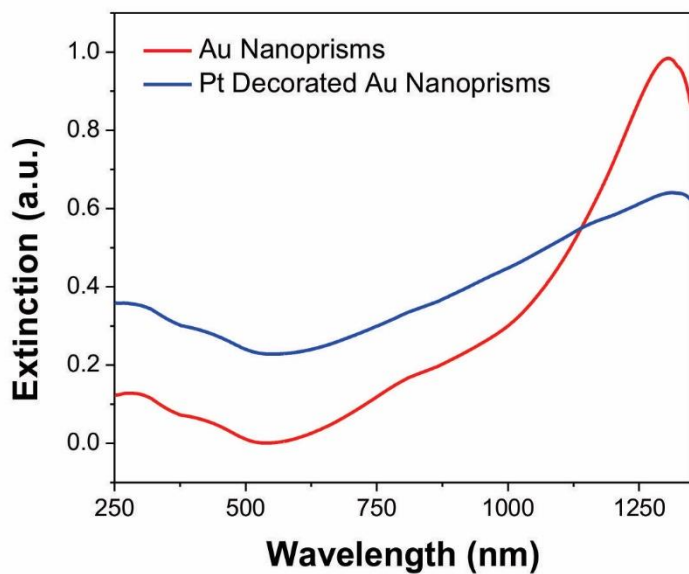


**Figure S7.** UV-Vis-NIR spectra depicting the difference in optical properties for Au nanoprisms before (red) and after (blue) Pt deposition. Here, deposition of Pt induces a damping of the in-plane dipole LSPR, as indicated by the increase in spectral breadth and decrease in intensity of approximately 30%.

#### S4. STEM-EELS of Additional Pt-Decorated Nanoprisms

Decomposition techniques are a powerful tool to characterize the plasmons in nanoparticles by fitting the entire, large, spectrum image. We chose to use non-negative matrix factorization (NMF), a blind-source separation approach.<sup>6-8</sup> In NMF, the main user input is the number of components to be extracted; the outputs include spectral components and their spatial distribution (loadings). The spectrum at each point in the spectrum image is fit by a linear combination of the components, the loadings being the coefficients of the components in the linear combination.

Below are results from additional Pt-decorated Au nanoprisms, as well as systematic analysis of that in Figures 6 and 7 of the manuscript. These figures are included here to show that the user input, i.e., the number of components, does not affect the position and spatial distribution of the corner and edge LSPRs extracted, as long as this number is large enough (see in particular the truncated Pt-decorated Au nanoprism in Figures S13-15).

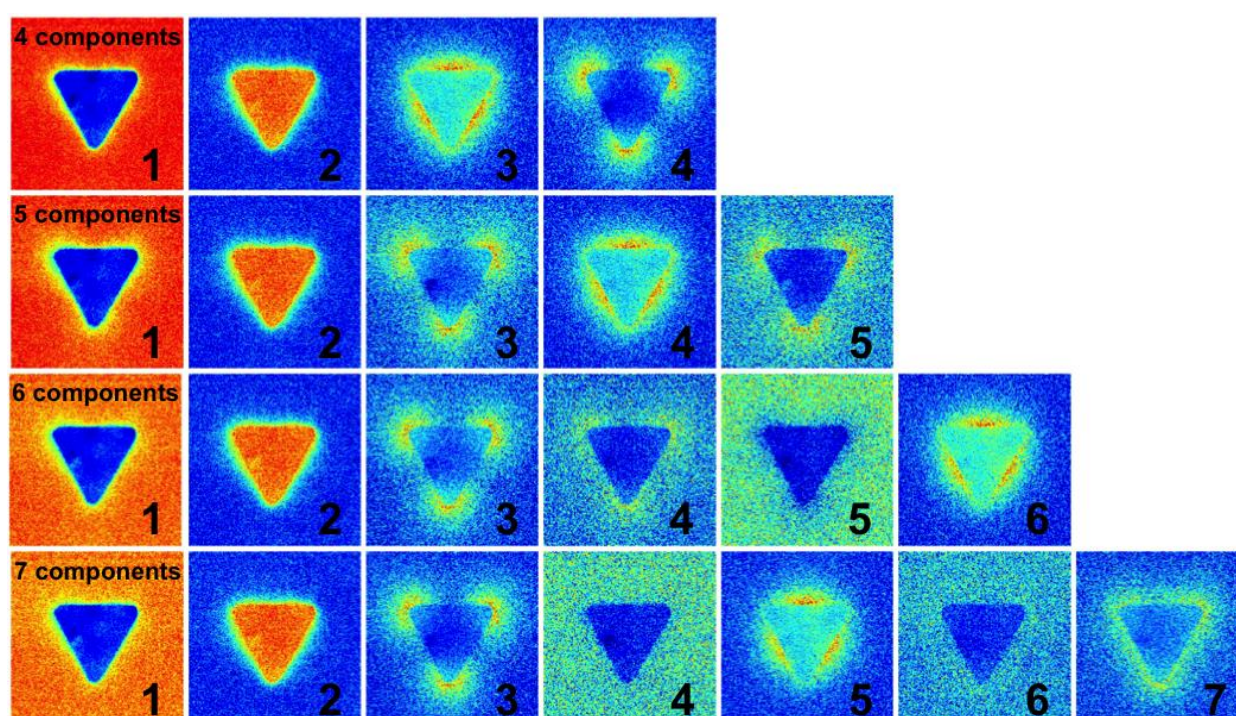


**Figure S8.** Systematic study of the effect of the number of components extracted in NMF analysis for the Pt-decorated Au nanoprism shown in Figures 6 and 7. Notice that the spatial distribution of the IBTs component, corner LSPR, and edge LSPR remain constant regardless of the number of components extracted.

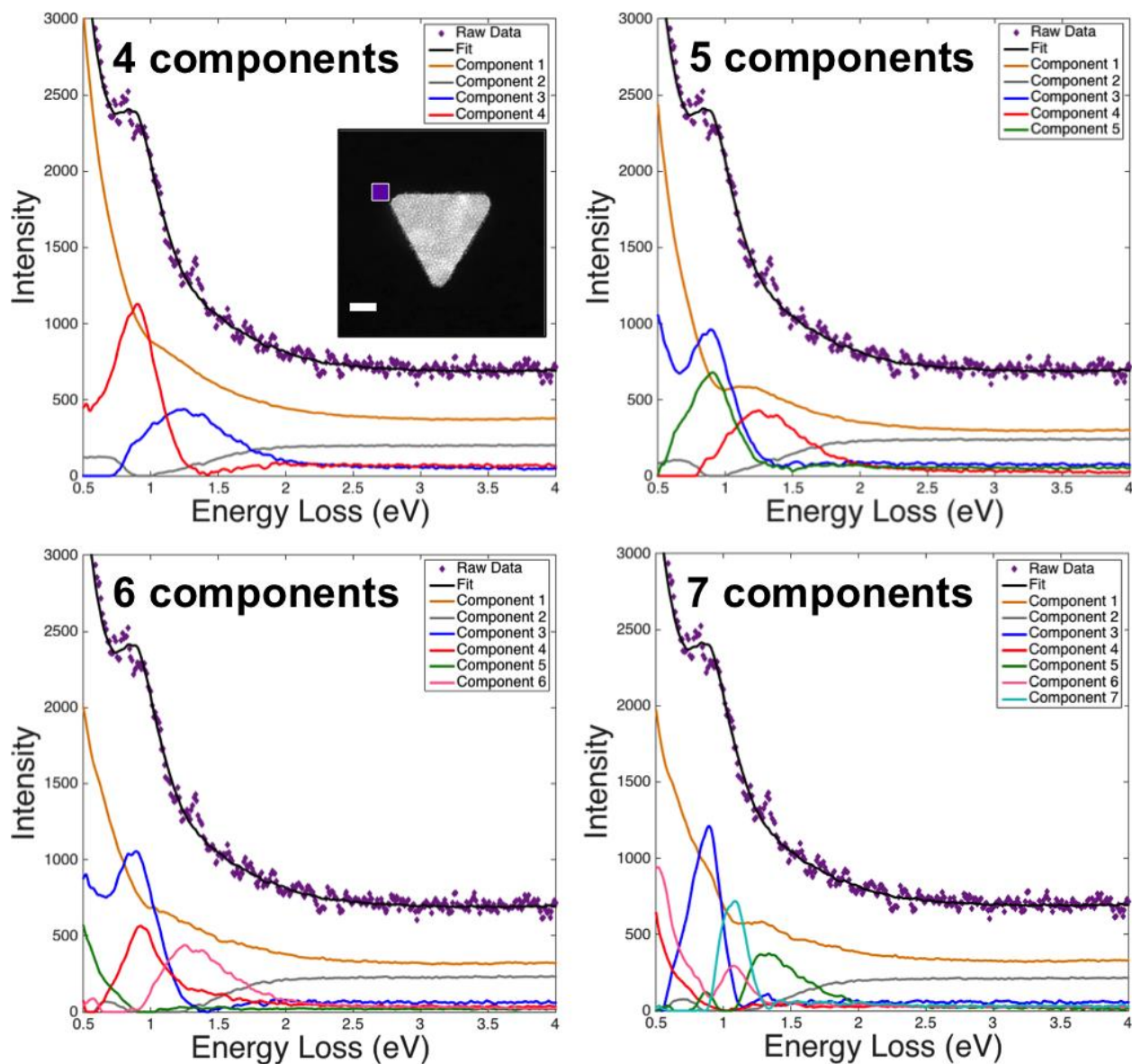


**Figure S9.** Spectral components obtained from NMF decomposition with different numbers of components, for the Pt-decorated Au nanoprism in Figures 6 and 7, at the position marked in the inset (binned  $5 \times 5$  pixels,  $9.3 \times 9.3$  nm; inset purple marker size exaggerated for clarity). Notice that the energy of the IBTs component, corner LSPR, and edge LSPR remain constant regardless of the number of components extracted. When extracting more components, the variation in the ZLP is increasingly fitted with the additional components.

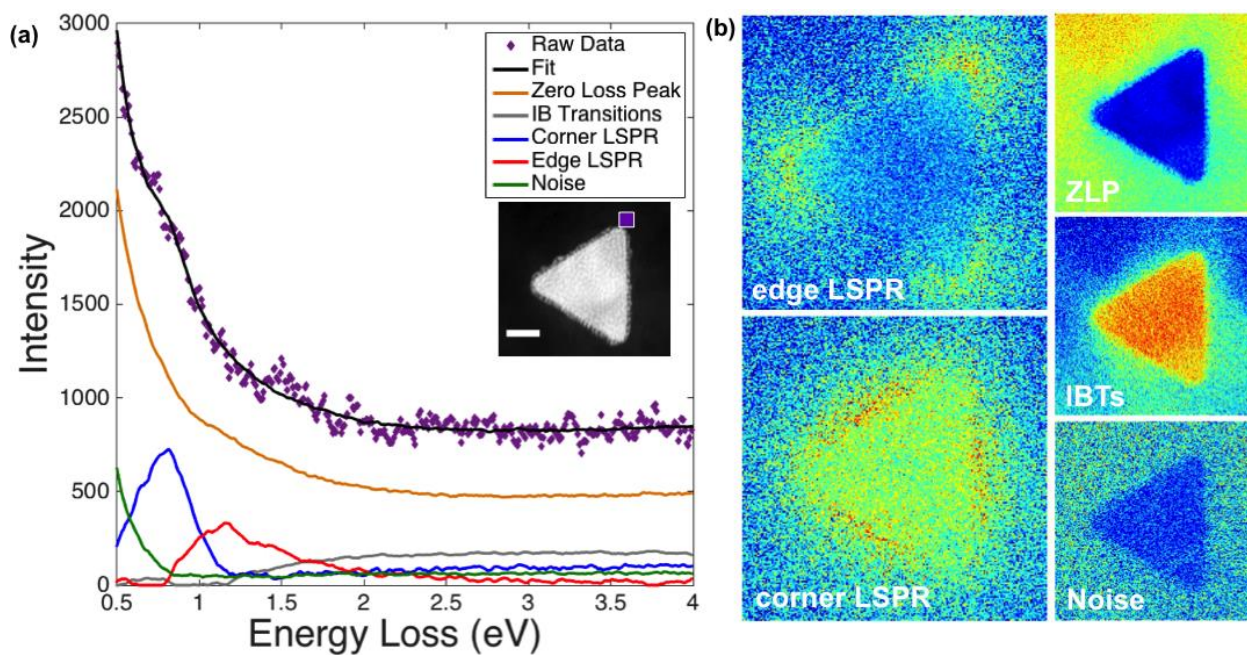


**Figure S10.** LSPRs and other contributions to EELS spectrum imaging of a single Pt-decorated Au nanoprism (extracted from a  $200 \times 200$  pixel by 2048 energy channel spectrum image, cropped to energy range 0.3-4.0 eV). (a) NMF-extracted spectral components and fit of the raw data for the EELS response at the position in the inset ( $5 \times 5$  pixels,  $6.4 \times 6.4$  nm, inset purple marker size exaggerated for clarity). (b) Spatial loadings of each of the components across the full spectrum image; edge LSPR, corner LSPR, zero loss peak (ZLP), interband transitions (IBTs) and noise. Scale bar, 50 nm.

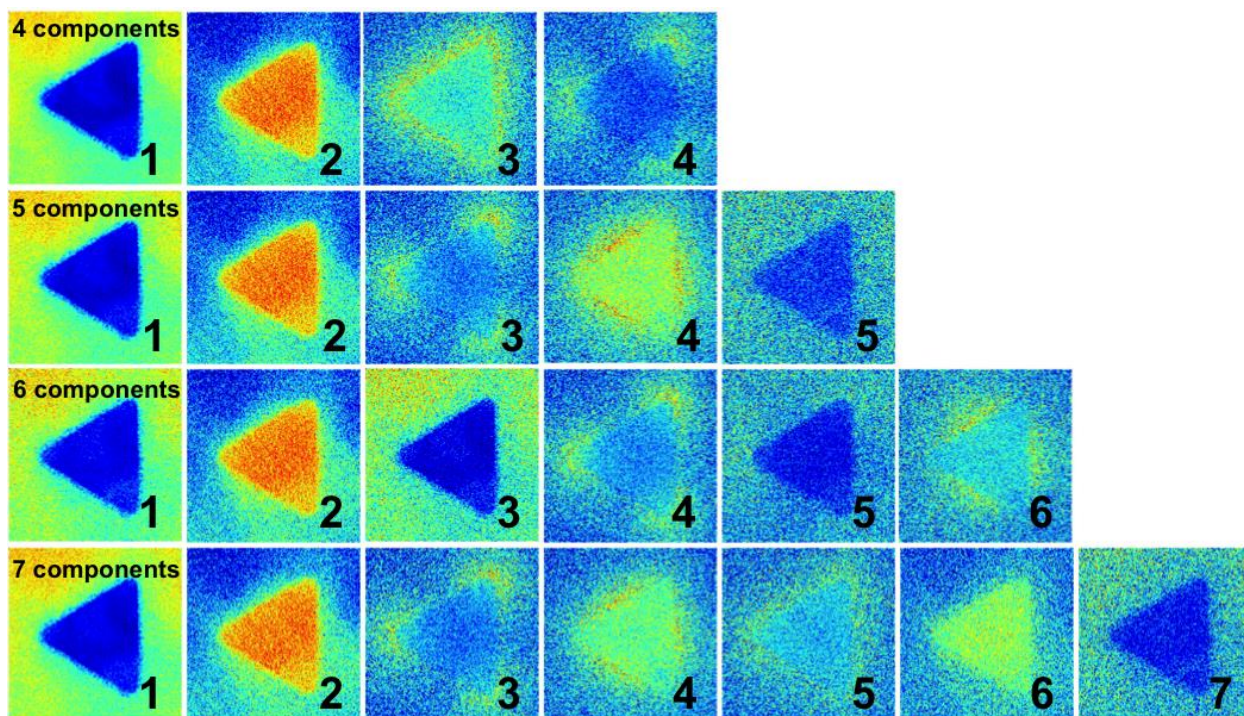


**Figure S11.** Systematic study of the effect of the number of components extracted in NMF analysis for the Pt-decorated Au nanoprism shown in Figure S10. Notice that the spatial distribution of the IBTs component, corner LSPR, and edge LSPR remain constant regardless of the number of components extracted.

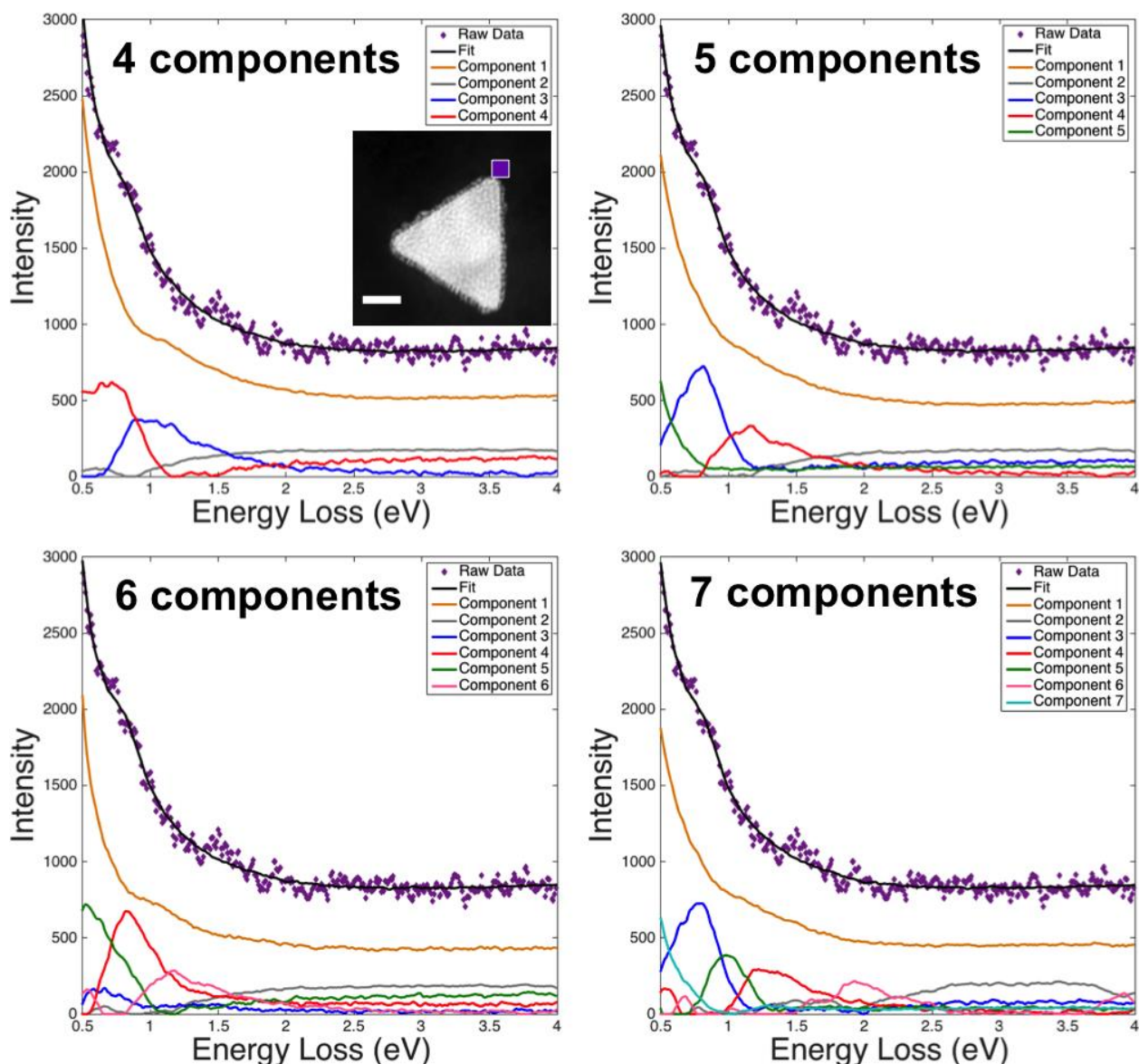


**Figure S12.** Spectral components obtained from NMF decomposition with different numbers of components, for the Pt-decorated Au nanoprism in Fig. S10, at the position marked in the inset (binned  $5 \times 5$  pixels,  $6.4 \times 6.4$  nm; inset purple marker size exaggerated for clarity). Notice that the energy of the IBTs component, corner LSPR, and edge LSPR remain constant regardless of the number of components extracted. When extracting more components, the variation in the ZLP is increasingly fitted with the additional components.

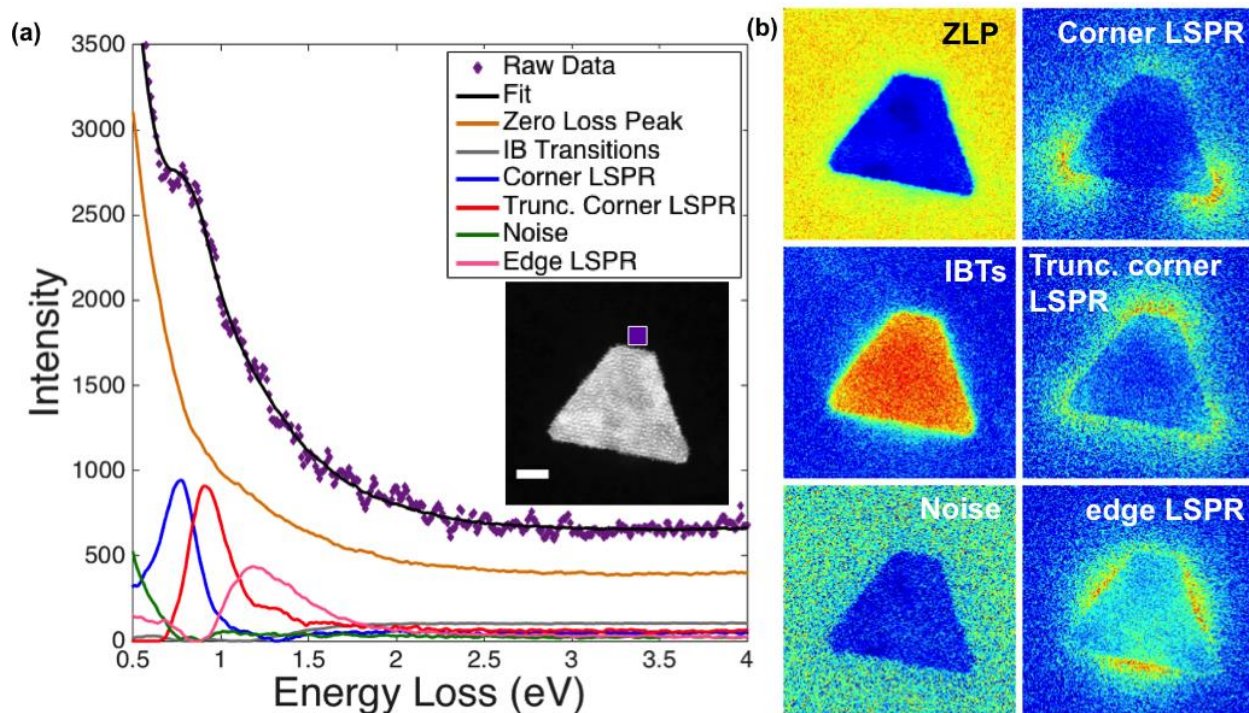


**Figure S13.** LSPRs and other contributions to EELS spectrum imaging of a single Pt-decorated Au nanoprism (extracted from a  $200 \times 200$  pixel by 2048 energy channel spectrum image, cropped to energy range 0.2-5.0 eV). (a) NMF-extracted spectral components and fit of the raw data for the EELS response at the position in the inset ( $5 \times 5$  pixels,  $8.5 \times 8.5$  nm, inset purple marker size exaggerated for clarity). (b) Spatial loadings of each of the components across the full spectrum image; edge LSPR, corner LSPR, zero loss peak (ZLP), interband transitions (IBTs) and noise. Scale bar, 50 nm.

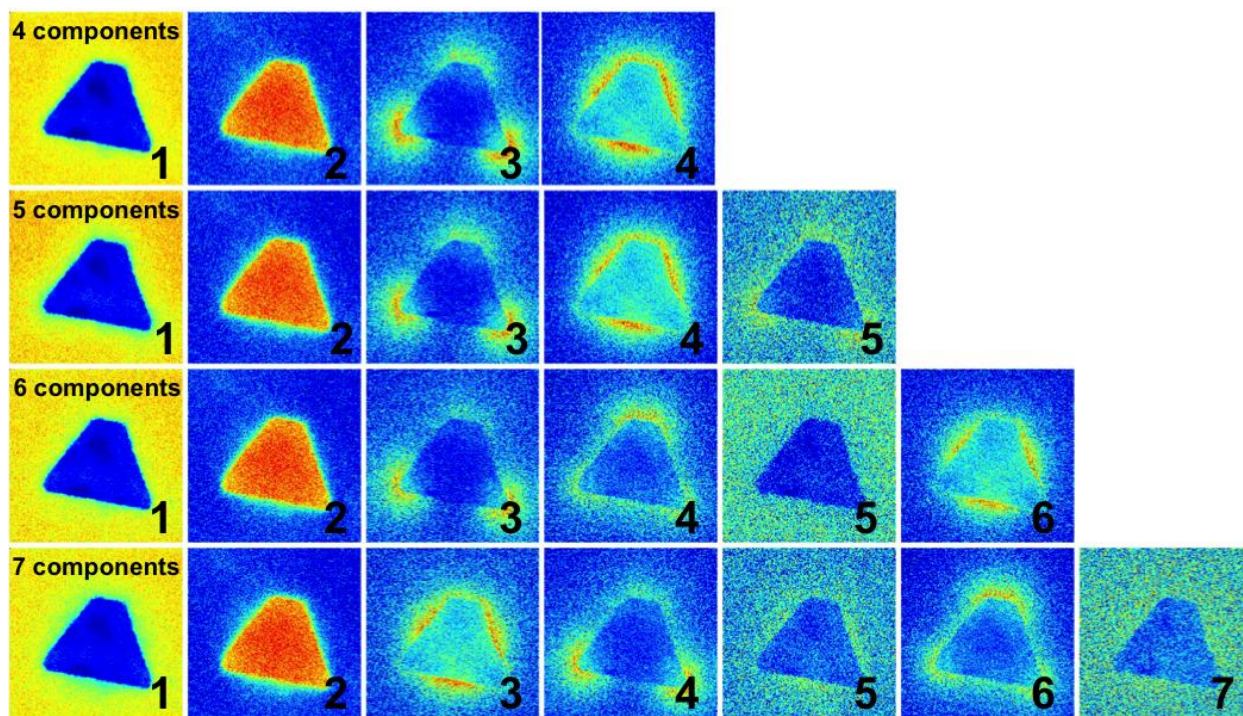


**Figure S14.** Systematic study of the effect of the number of components extracted in NMF analysis for the truncated Pt-decorated Au nanoprism shown in Figure S13. Notice that the spatial distribution of the IBTs component, corner LSPR, and edge LSPR remain mostly constant regardless of the number of components extracted. However, extracting fewer components leads to combining the truncated corner and corner LSPRs (they are 6 components (panels 3, 4) and 7 components (4, 7), while they are combined in 5 components (3) and 4 components (3)).

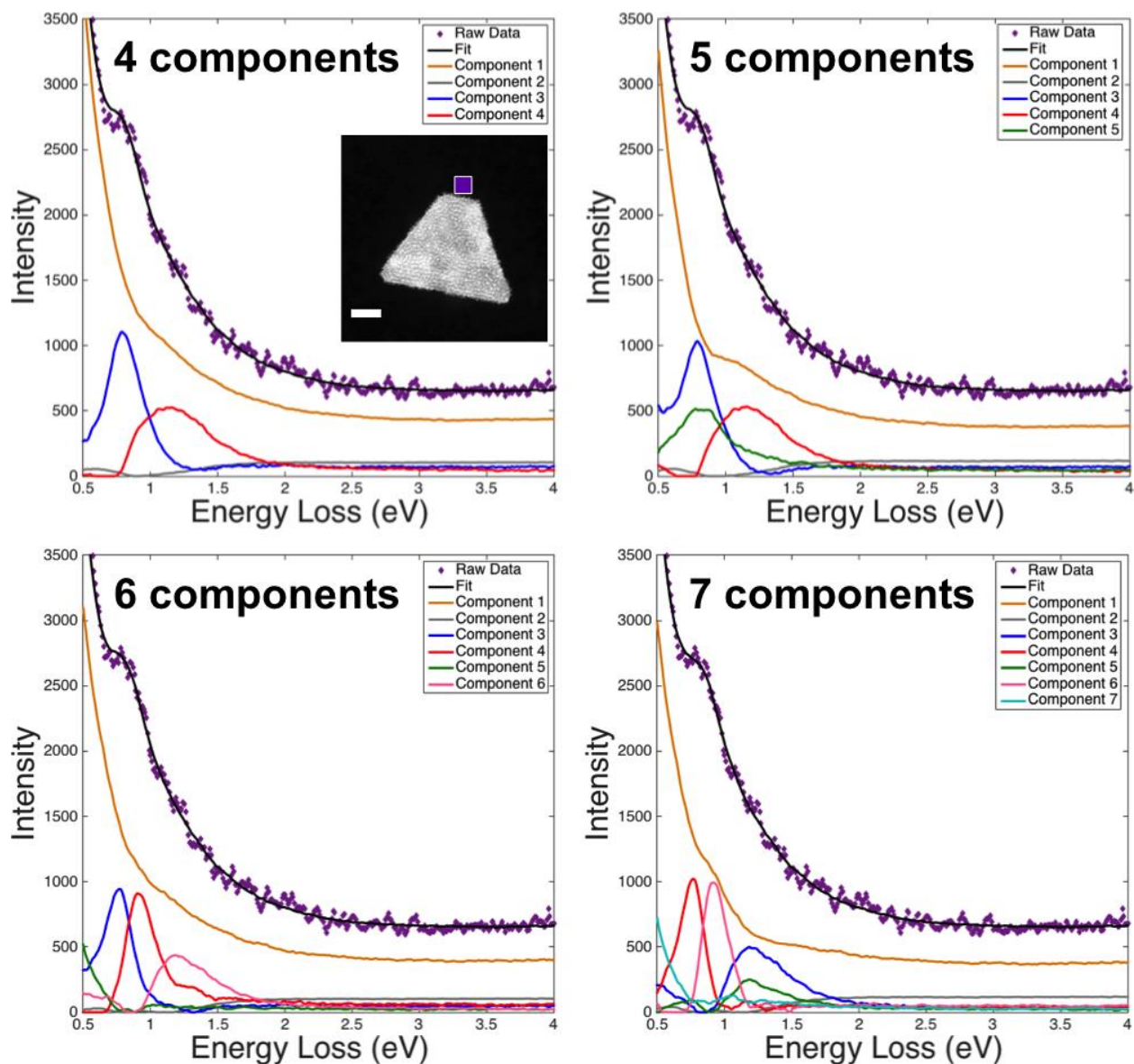


**Figure S15.** Spectral components obtained from NMF decomposition with different numbers of components, for the Pt-decorated Au nanoprism in Fig. S13, at the position marked in the inset (binned  $5 \times 5$  pixels,  $8.5 \times 8.5$  nm; inset purple marker size exaggerated for clarity). Notice that the energy of the IBTs component, corner LSPR, and edge LSPR remain constant regardless of the number of components extracted. When extracting more components, the variation in the ZLP is increasingly fitted with the additional components.

#### **S4. STEM-EELS of Undecorated Au Nanoprisms**

As a control experiment to demonstrate that the decorated prisms sustain the same LSPRs as undecorated prisms, STEM-EELS data of undecorated Au nanoprisms was obtained and analyzed in a similar manner. The undecorated Au nanoprisms were deposited on similar  $\text{Si}_3\text{N}_4$  membrane windows, and comparable EELS spectrometers were used. However, the acquisition time per pixel for the undecorated particles was set to 400 times higher for the undecorated prisms due to the availability of the new Titan Themis microscope at Rice University, significantly improving the signal/noise. The modes observed using the same data analysis methods as for the decorated nanoprisms (i.e. NMF, as described above) clearly indicate that the undecorated and decorated nanoprisms sustain the same corner and edge modes.

Briefly, Figures S16, S18 and S20 show analogous raw and fitted NMF spectral features to those in Figure 6 of the manuscript; that is, peaks at  $\sim 0.9$  and  $\sim 1.5$  eV when the beam passes close to the nanoprism corners or edges, respectively. Similarly, using a four component NMF decomposition for the full STEM-EELS spectrum images of the undecorated nanoprisms, shown in Figures S17, S19 and S21, reveal comparable energies and spatial distributions of corner and edge LSPRs to those of the decorated nanoprisms in Figures 7, S10 and S13. Inevitably, since there is some variation in size and shape between different nanoprisms (regardless of whether they are decorated or undecorated), there will be some small differences in these LSPRs.

We note that owing primarily to the much greater signal-to-noise ratio possible during the acquisition of data for the undecorated nanoprisms (due to the 400-fold increase in acquisition time), weak higher order LSPR modes are seen when using more than four NMF components. However, using more components does not alter the spatial distributions or energies of the corner and edge LSPRs seen in Figures S17, S19 and S21.

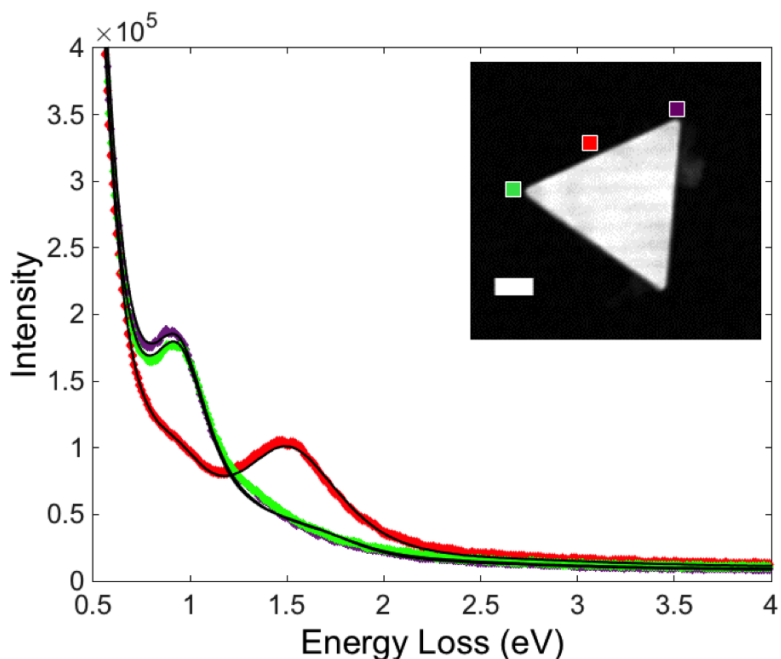


**Figure S16.** Raw (color-coded diamonds, binned  $5 \times 5$  pixels equivalent to  $15 \times 15$  nm) and fitted (linear combination of NMF-extracted components, black lines) EELS spectra obtained from an undecorated Au nanoprism, at the positions indicated by color-coded squares in the HAADF-STEM image (square sizes exaggerated for clarity). Scale bar, 50 nm.

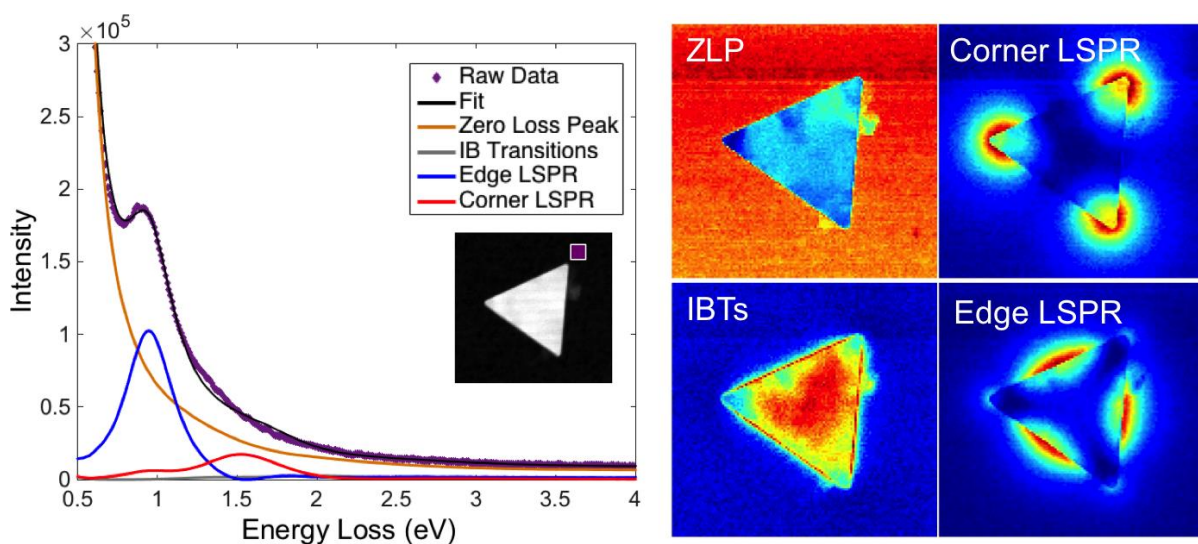


**Figure S17.** LSPRs and other contributions to EELS spectrum imaging of a single undecorated Au nanoprism (same as S16, extracted from a  $128 \times 121$  pixel by 2048 energy channel spectrum image, cropped to energy range 0.3-5.0 eV). (a) NMF-extracted spectral components and fit of the raw data for the EELS response at the position in the inset ( $5 \times 5$  pixels,  $15 \times 15$  nm, inset purple marker size exaggerated for clarity). (b) Spatial loadings of each of the components across the full spectrum image; edge LSPR, corner LSPR, zero loss peak (ZLP), interband transitions (IBTs) and noise. Scale bar, 50 nm.

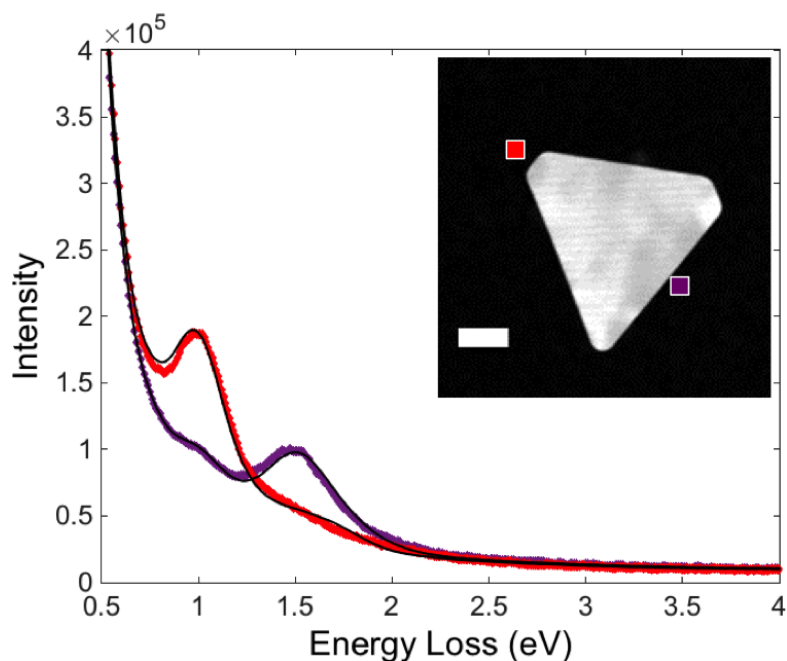


**Figure S18.** Raw (color-coded diamonds, binned  $5 \times 5$  pixels equivalent to  $13.6 \times 13.6$  nm) and fitted (linear combination of NMF-extracted components, black lines) EELS spectra obtained from an undecorated Au nanoprism, at the positions indicated by color-coded squares in the HAADF-STEM image (square sizes exaggerated for clarity). Scale bar, 50 nm.

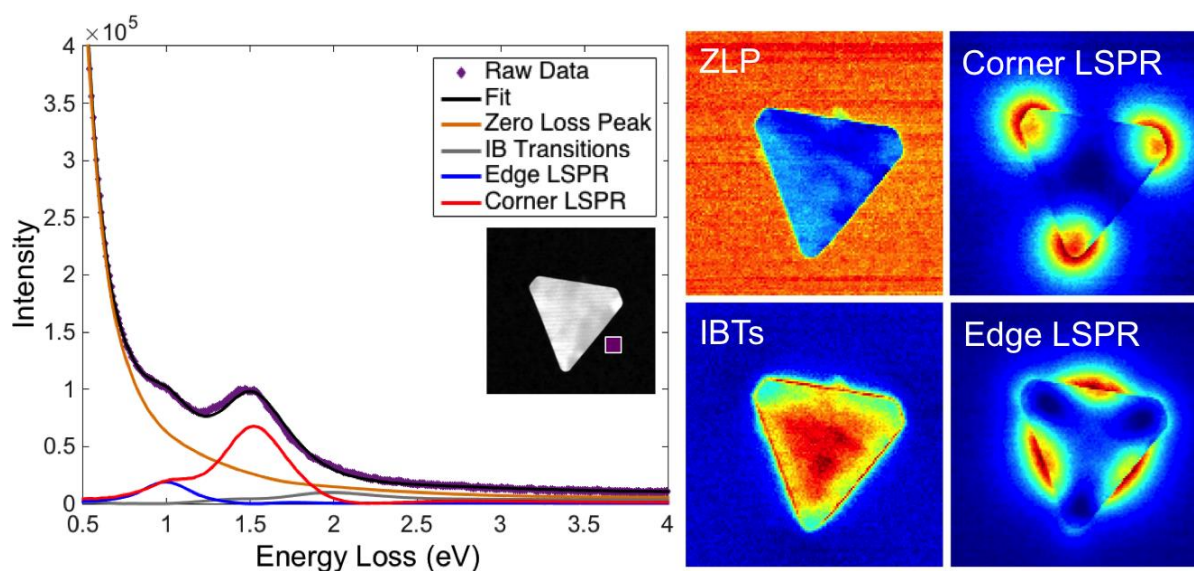


**Figure S19.** LSPRs and other contributions to EELS spectrum imaging of a single undecorated Au nanoprism (same as S18, extracted from a  $128 \times 131$  pixel by 2048 energy channel spectrum image, cropped to energy range 0.3-5.0 eV). (a) NMF-extracted spectral components and fit of the raw data for the EELS response at the position in the inset ( $5 \times 5$  pixels,  $13.6 \times 13.6$  nm, inset purple marker size exaggerated for clarity). (b) Spatial loadings of each of the components across the full spectrum image; edge LSPR, corner LSPR, zero loss peak (ZLP), interband transitions (IBTs) and noise. Scale bar, 50 nm.

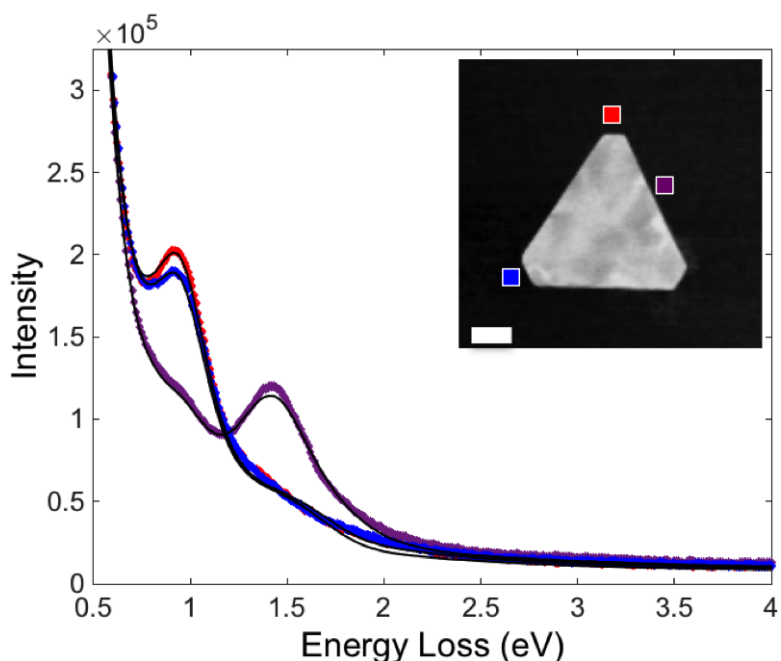


**Figure S20.** Raw (color-coded diamonds, binned  $5 \times 5$  pixels equivalent to  $14 \times 14$  nm) and fitted (linear combination of NMF-extracted components, black lines) EELS spectra obtained from an undecorated Au nanoprism, at the positions indicated by color-coded squares in the HAADF-STEM image (square sizes exaggerated for clarity). Scale bar, 50 nm.

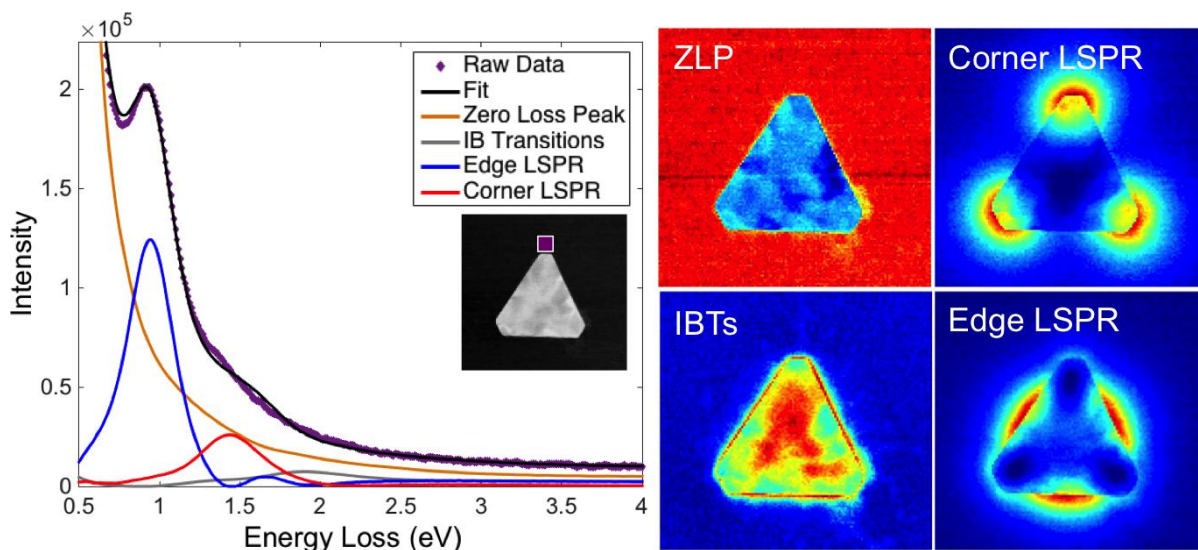


**Figure S21.** LSPRs and other contributions to EELS spectrum imaging of a single undecorated Au nanoprism (same as S20, extracted from a  $143 \times 127$  pixel by 2048 energy channel spectrum image, cropped to energy range 0.3-5.0 eV). (a) NMF-extracted spectral components and fit of the raw data for the EELS response at the position in the inset ( $5 \times 5$  pixels,  $14 \times 14$  nm, inset purple marker size exaggerated for clarity). (b) Spatial loadings of each of the components across the full spectrum image; edge LSPR, corner LSPR, zero loss peak (ZLP), interband transitions (IBTs) and noise. Scale bar, 50 nm.

## REFERENCES

- (1) Midgley, P. A.; Weyland, M., 3D Electron Microscopy in the Physical Sciences: the Development of Z-Contrast and EFTEM Tomography. *Ultramicroscopy* **2003**, *96*, 413-431.
- (2) Leary, R.; Saghi, Z.; Midgley, P. A.; Holland, D. J., Compressed Sensing Electron Tomography. *Ultramicroscopy* **2013**, *131*, 70-91.
- (3) Goris, B.; Van den Broek, W.; Batenburg, K. J.; Heidari Mezerji, H.; Bals, S., Electron Tomography Based on a Total Variation Minimization Reconstruction Technique. *Ultramicroscopy* **2012**, *113*, 120-130.
- (4) van Aarle, W.; Palenstijn, W. J.; De Beenhouwer, J.; Altantzis, T.; Bals, S.; Batenburg, K. J.; Sijbers, J., The ASTRA Toolbox: A Platform for Advanced Algorithm Development in Electron Tomography. *Ultramicroscopy* **2015**, *157*, 35-47.
- (5) Li, C.; Yin, W.; Jiang, H.; Zhang, Y., An Efficient Augmented Lagrangian Method with Applications to Total Variation Minimization. *Comput. Optim. Appl.* **2013**, *56*, 507-530.
- (6) Ringe, E.; DeSantis, C. J.; Collins, S. M.; Duchamp, M.; Dunin-Borkowski, R. E.; Skrabalak, S. E.; Midgley, P. A., Resonances of Nanoparticles with Poor Plasmonic Metal Tips. *Sci. Rep.* **2015**, *5*, 17431.
- (7) Collins, S. M.; Ringe, E.; Duchamp, M.; Saghi, Z.; Dunin-Borkowski, R. E.; Midgley, P. A., Eigenmode Tomography of Surface Charge Oscillations of Plasmonic Nanoparticles by Electron Energy Loss Spectroscopy. *ACS Photon.* **2015**, *2*, 1628-1635.
- (8) Nicoletti, O.; de La Peña, F.; Leary, R. K.; Holland, D. J.; Ducati, C.; Midgley, P. A., Three-Dimensional Imaging of Localized Surface Plasmon Resonances of Metal Nanoparticles. *Nature* **2013**, *502*, 80-84.